Draft version March 8, 2021
Typeset using LaTeX **twocolumn** style in AASTeX63

The discovery of a highly accreting, radio-loud quasar at $z = 6.82$

Eduardo Bañados [1,2] Chiara Mazzucchelli [3,*] Emmanuel Momjian [4] Anna-Christina Eilers [5,†] Feige Wang [6,†] Jan-Torge Schindler [1] Thomas Connor [7] Irham Taufik Andika [1,8] Aaron J. Barth [9] Chris Carilli [4,10] Frederick B. Davies [1] Roberto Decarli [11] Xiaohui Fan [12] Emanuele Paolo Farina [13] Joseph F. Hennawi [14] Antonio Pensabene [15,11] Daniel Stern [7] Bram P. Venemans [1] Lukas Wenzl [16,1] and Jinyi Yang [12,‡]

[1] *Max Planck Institut für Astronomie, Königstuhl 17, D-69117, Heidelberg, Germany*
[2] *The Observatories of the Carnegie Institution for Science, 813 Santa Barbara Street, Pasadena, CA 91101, USA*
[3] *European Southern Observatory, Alonso de Cordova 3107, Vitacura, Region Metropolitana, Chile*
[4] *National Radio Astronomy Observatory, Pete V. Domenici Science Operations Center, P.O. Box O, Socorro, NM 87801, USA*
[5] *MIT Kavli Institute for Astrophysics and Space Research, 77 Massachusetts Ave., Cambridge, MA 02139, USA*
[6] *Steward Observatory, University of Arizona, 933 North Cherry Avenue, Tucson, AZ 85721, USA*
[7] *Jet Propulsion Laboratory, California Institute of Technology, 4800 Oak Grove Drive, Pasadena, CA 91109, USA*
[8] *International Max Planck Research School for Astronomy & Cosmic Physics at the University of Heidelberg, Germany*
[9] *Department of Physics and Astronomy, 4129 Frederick Reines Hall, University of California, Irvine, CA, 92697-4575, USA*
[10] *Astrophysics Group, Cavendish Laboratory, J.J. Thomson Avenue, Cambridge CB3 0HE, UK*
[11] *INAF — Osservatorio di Astrofisica e Scienza dello Spazio, via Gobetti 93/3, I-40129, Bologna, Italy*
[12] *Steward Observatory, University of Arizona, 933 N Cherry Ave, Tucson, AZ, USA*
[13] *Max Planck Institut für Astrophysik, Karl-Schwarzschild-Straße 1, D-85748, Garching bei München, Germany*
[14] *Department of Physics, Broida Hall, University of California, Santa Barbara, CA 93106–9530, USA*
[15] *Dipartimento di Fisica e Astronomia, Alma Mater Studiorum, Università di Bologna, Via Gobetti 93/2, I-40129 Bologna, Italy.*
[16] *Department of Astronomy, Cornell University, Ithaca, NY 14853, USA*

(Accepted January 31, 2021)

ABSTRACT

Radio sources at the highest redshifts can provide unique information on the first massive galaxies and black holes, the densest primordial environments, and the epoch of reionization. The number of astronomical objects identified at $z > 6$ has increased dramatically over the last few years, but previously only three radio-loud ($R_{2500} = f_{\nu,5\,\mathrm{GHz}}/f_{\nu,2500\,\text{Å}} > 10$) sources had been reported at $z > 6$, with the most distant being a quasar at $z = 6.18$. Here we present the discovery and characterization of PSO J172.3556+18.7734, a radio-loud quasar at $z = 6.823$. This source has an Mg II-based black hole mass of $\sim 3 \times 10^8\,M_\odot$ and is one of the fastest accreting quasars, consistent with super-Eddington accretion. The ionized region around the quasar is among the largest measured at these redshifts, implying an active phase longer than the average lifetime of the $z \gtrsim 6$ quasar population. From archival data, there is evidence that its 1.4 GHz emission has decreased by a factor of two over the last two decades. The quasar's radio spectrum between 1.4 and 3.0 GHz is steep ($\alpha = -1.31$). Assuming the measured radio slope and extrapolating to rest-frame 5 GHz, the quasar has a radio-loudness parameter $R_{2500} \sim 90$. A second steep radio source ($\alpha = -0.83$) of comparable brightness to the quasar is only 23.″1 away (∼120 kpc at $z = 6.82$; projection probability $< 2\%$), but shows no optical or near-infrared counterpart. Further follow-up is required to establish whether these two sources are physically associated.

Corresponding author: Eduardo Bañados
banados@mpia.de

Keywords: Radio loud quasars (1349); Quasars (1349); Active galactic nuclei (16); Extragalactic radio sources (508); Supermassive black holes (1663)

1. INTRODUCTION

Radio jets from active galactic nuclei (AGNs) are thought to play a key role in the coevolution of supermassive black holes and their host galaxies, as well as in the early growth of massive black holes (e.g., Jolley & Kuncic 2008; Volonteri et al. 2015; Hardcastle & Croston 2020). Yet, strong radio emission seems to be a rare or at least short-lived phenomenon. Only about 10% of all quasars are strong radio emitters, almost independent of their redshifts up to $z \sim 6$ (e.g., Bañados et al. 2015; Yang et al. 2016; Shen et al. 2019 but see also Jiang et al. 2007; Kratzer & Richards 2015).

The radio-loudness of a quasar is usually defined as the ratio of rest-frame 5 GHz (radio) and 4400 Å (optical) flux densities (R_{4400}; e.g., Kellermann et al. 1989) although sometimes the 2500 Å (UV) emission is used instead of the optical flux density (R_{2500}; e.g., Jiang et al. 2007). For an unobscured type-1 quasar, the different definitions yield comparable results. An object is considered radio-loud[1] if R_{2500} or R_{4400} is greater than 10. Radio-loud sources at the highest accessible redshifts are of particular interest for multiple reasons. For example, radio galaxies are known to be good tracers of overdense environments (e.g., Venemans et al. 2007; Wylezalek et al. 2013) and at high redshift these overdensities could be the progenitors of the galaxy clusters seen in the present-day universe (Overzier 2016; Noirot et al. 2018). Furthermore, radio-loud sources deep in the epoch of reionization would enable crucial absorption studies of the intergalactic medium (IGM) at this critical epoch (e.g., Carilli et al. 2002; Ciardi et al. 2013; Thyagarajan 2020) and they could potentially also constrain the nature of dark matter particles by detecting neutral hydrogen in absorption in the radio spectrum (e.g., Shimabukuro et al. 2020).

The number of astronomical objects known within the first billion years of the universe has increased dramatically over the last few years, with galaxies being discovered up to $z \sim 11$ (Oesch et al. 2014) and quasars up to $z \sim 7.5$ (Bañados et al. 2018b; Yang et al. 2020). On the other hand, identifying strong radio emitters at high redshift has been difficult. The highest-redshift radio galaxy lies at $z = 5.7$ (Saxena et al. 2018), with the previous record at $z = 5.2$ (van Breugel et al. 1999). Out of the 200 published quasars at $z > 6$ (e.g., Bañados et al. 2016; Matsuoka et al. 2019a; Andika et al. 2020), only three are known to be radio-loud. For the large majority of the remainder, the existing radio data are too shallow to robustly classify them as radio-quiet or radio-loud, although there are on-going efforts to obtain deeper radio observations of these objects. The three $z > 6$ radio-loud quasars currently known[2], listed by increasing redshift, are: J0309+2717 at $z = 6.10$ (Belladitta et al. 2020), J1427+3312 at $z = 6.12$ (McGreer et al. 2006; Stern et al. 2007), and J1429+5447 at $z = 6.18$ (Willott et al. 2010a).

In this paper we present the discovery and initial characterization of the most distant radio-loud quasar currently known, PSO J172.3556+18.7734 (hereafter P172+18) at $z = 6.823$, as measured from the Mg II emission line. In Section 2 we describe the selection of the quasar and the details of follow-up observations. The properties derived from near-infrared spectroscopy are presented in Section 3 and the properties from follow-up radio observations are introduced in Section 4. We summarize and present our conclusion in Section 5. Throughout the paper we use a flat cosmology with $H_0 = 70\,\mathrm{km\,s^{-1}\,Mpc^{-1}}$, $\Omega_M = 0.3$, and $\Omega_\Lambda = 0.7$. In this cosmology the age of the universe at the redshift of P172+18 is 776 Myr and 1 pkpc corresponds to 5.″3. Optical and near-infrared magnitudes are reported in the AB system, while for radio observations we report the peak flux density unless otherwise stated. For nondetections we report 3σ upper limits.

2. A RADIO-LOUD QUASAR AT $z = 6.8$

2.1. *Selection and Discovery*

P172+18 has been identified as a $z > 6.5$ quasar candidate by at least two independent methods. We first selected P172+18 as a z-dropout radio-loud candidate in Bañados et al. 2015 (see their Table 1). That selection required red ($z_{\rm P1} - y_{\rm P1} > 1.4$) sources in the

* ESO Fellow
† NASA Hubble Fellow
‡ Strittmatter Fellow

[1] When we talk about radio-loud quasars in this paper we refer to jetted-quasars, see discussion in Padovani (2017)

[2] The quasar J1609+3041 at $z = 6.14$ was classified as radio-loud by Bañados et al. (2015) based on a tentative 1.4 GHz detection at S/N of 3.5. However, deeper observations showed this object to be radio-quiet (Liu et al. 2021). Also note that Liu et al. (2021) detected the quasar J0227–0605 at $z = 6.2$ at 3 GHz but not at 1.4 GHz, making it potentially radio-loud, though deeper 1.4 GHz (or lower frequency) observations are required for a robust classification.

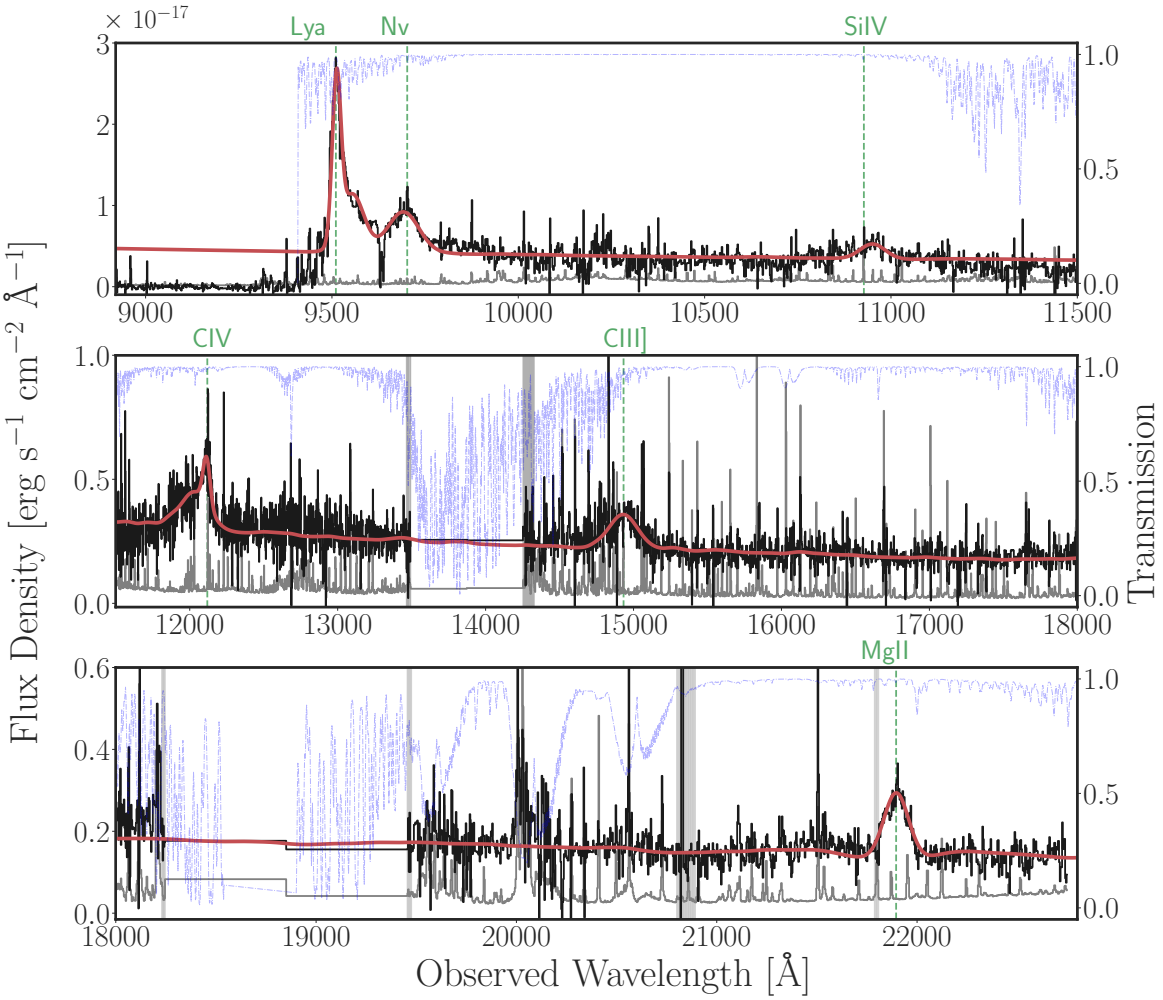

Figure 1. Optical/near-infrared spectrum of P172+18. The final spectrum was obtained by combining all the spectroscopic follow-up data available (Keck/NIRES, VLT/X-Shooter, and LBT/MODS).

stacked object Pan-STARRS1 catalog (Chambers et al. 2016) and a counterpart in the radio survey Faint Images of the Radio Sky at Twenty cm (FIRST, Becker et al. 1995) to avoid most of the L- and T-dwarfs, which are the main contaminants for $z > 6.5$ quasar searches (see Bañados et al. 2015 for details). The Pan-STARRS1 and FIRST measurements for P172+18 are listed in Table 1. This object also stands out as a promising high-redshift quasar candidate in a new method to select $z \gtrsim 6.5$ quasars exploiting the overlap of Pan-STARRS1 and the DESI Legacy Imaging Surveys (DECaLS; Dey et al. 2019), which will be presented in a forthcoming paper along with additional $z \gtrsim 6.5$ quasar discoveries (E. Bañados et al. in preperation). P172+18 was selected using the DECaLS DR7 catalog, but in Table 1 we report the photometry from the latest (DR8) data release.

The optical photometry of P172+18 in the DECaLS DR7 and DR8 catalogs is consistent. However, the mid-infrared Wide-fied Infrared Survey Explorer (*WISE*) magnitudes are inconsistent[3] at the 2σ level even though DR7 and DR8 use the same input set of *WISE* images spanning from 2010 to 2017 (A. Meisner, private communication; Meisner et al. 2019). DECaLS provides matched *WISE* photometry by using the $g_{\rm DE}$, $r_{\rm DE}$, $z_{\rm DE}$ information to infer the *WISE* magnitudes from deep image coadds using all available *WISE* data (Lang 2014; Meisner et al. 2017, 2019). The *WISE* DECaLS DR7 magnitudes are $W1 = 21.25 \pm 0.21$ and $W2 = 21.30 \pm 0.51$ in contrast to the DR8 magnitudes of $W1 = 20.71 \pm 0.13$ and $W2 = 20.73 \pm 0.31$. The main difference between DR7 and DR8 is the change of sky modeling as presented in Schlafly et al. (2019), which can affect the fluxes of sources at the faint limit

[3] We also note that P172+18 does not appear in the ALLWISE (Cutri 2014), unWISE (Schlafly et al. 2019), or CatWISE (Eisenhardt et al. 2020) catalogs.

of the unWISE coadds. Therefore, the reported *WISE* magnitudes need to be taken with caution.

We confirmed P172+18 as a $z \sim 6.8$ quasar on 2019 January 12 with a 450 s spectrum using the Folded-port InfraRed Echellete (FIRE; Simcoe et al. 2008, 2013) spectrograph in prism mode at the Magellan Baade telescope at Las Campanas Observatory. The spectrum had poor signal-to-noise ratio (S/N) but was sufficient to unequivocally identify P172+18 as the most distant radio-loud quasar known to date, which triggered a number of follow-up programs described below.

2.2. *Near-infrared Imaging Follow-up*

We obtained JHK photometry using the NOTCam instrument at the Nordic Optical Telescope (Djupvik & Andersen 2010). The total exposure times were 19 minutes each for $J_{\rm NOT}$ and $H_{\rm NOT}$ and 31 minutes for $Ks_{\rm NOT}$. Data reduction consisted of standard procedures: bias subtraction, flat-fielding, sky subtraction, alignment, and stacking. Table 2 presents a log of the observations.

We calculate the zero-points of the NOT observations, calibrating against stars in the Two Micron All Sky Survey (2MASS) using the following conversions:

$$J_{\rm NOT} = J_{\rm 2MASS} - 0.074 \times (J_{\rm 2MASS} - H_{\rm 2MASS}) + 0.003$$
$$H_{\rm NOT} = H_{\rm 2MASS} + 0.045 \times (J_{\rm 2MASS} - H_{\rm 2MASS}) + 0.006$$
$$Ks_{\rm NOT} = K_{\rm 2MASS} + 0.580 \times (H_{\rm 2MASS} - K_{\rm 2MASS}) + 0.225$$

These conversions were calculated via linear fits of the stellar loci as described in Section 2.6 of Bañados et al. (2014). The near-infrared photometry is listed in Table 1.

2.3. *Spectroscopic Follow-up*

We obtained three follow-up spectra of P172+18. On 2019 February 18 we observed P172+18 for 3.5 hr with Keck/NIRES (Wilson et al. 2004). Between 2019 March 8 and April 8 we used the Very Lare Telescope (VLT)/X-Shooter spectrograph (Vernet et al. 2011) to observe the target for a total time of 3.5 hr. We also observed P172+18 with the Large Binocular Telescope (LBT)/Multi-Object Double Spectrograph (MODS) (Pogge et al. 2010) on 2019 June 13. The MODS observations were carried out in binocular mode for 20 minutes on-source. We summarize the spectroscopic follow-up observations in Table 3.

The Keck/NIRES and VLT/X-Shooter data were reduced with the Python Spectroscopic Data Reduction Pipeline (PypeIt; Prochaska et al. 2019; Prochaska et al. 2020). In practice, sky subtraction on the 2D images was obtained through a B-spline fitting procedure and differences between AB dithered exposures. The 1D spectrum was extracted with the optimal spectrum extraction technique (Horne 1986). Each 1D single exposure was flux-calibrated using standard stars observed with X-Shooter. Then, the 1D spectra were stacked and a telluric model was fitted, obtained from telluric model grids from the Line-By-Line Radiative Transfer Model (LBLRTM4; Clough et al. 2005, Gullikson et al. 2014). The X-Shooter and NIRES spectra were then absolute-flux-calibrated with respect to the $J_{\rm NOT}$ magnitude (see Table 1). The LBT/MODS binocular spectra were reduced with IRAF using standard procedures, including bias subtraction, flat-fielding, and telluric and wavelength calibration. They were each scaled to the $y_{\rm P1}$ magnitude.

We performed all measurements presented in the following sections in the individual spectra, which resulted in consistent results. To maximize the information provided by all spectra we re-binned them to a common wavelength grid with a pixel size of $50\,{\rm km\,s^{-1}}$, and averaged them weighting by their inverse variance. The final spectrum that we use for our main analysis is shown in Figure 1 and a zoom-in on the main emission lines is presented in Figure 2.

2.4. *Radio Follow-up*

Follow-up radio-frequency observations were carried out with the Karl G. Jansky Very Large Array (VLA) of the NRAO[4] on 2019 March 5 and 2019 March 11, in S and L bands respectively. Each observing session was 1 hr in total (∼21 min on-source). The VLA was in B-configuration with a maximum baseline length of 11.1 km. The observations spanned the frequency ranges 1–2 GHz (L band; center frequency 1.5 GHz) and 2–4 GHz (S band; center frequency 3 GHz). The WIDAR correlator was configured to deliver 16 adjacent subbands per receiver band, each 64 MHz at L band and 128 MHz at S band. Each subband had 64 spectral channels, resulting in 1 MHz channels in the L-band data and 2 MHz channels in the S-band data.

The source 3C 286 (J1331+3030) was used to set the absolute flux density scale and to calibrate the bandpass response, and the compact source J1120+1420 was observed as the complex gain calibrator. Data editing, radio-frequency interference (RFI) excision, calibration, imaging, and analysis were performed using the Com-

[4] The National Radio Astronomy Observatory is a facility of the National Science Foundation operated under cooperative agreement by Associated Universities, Inc.

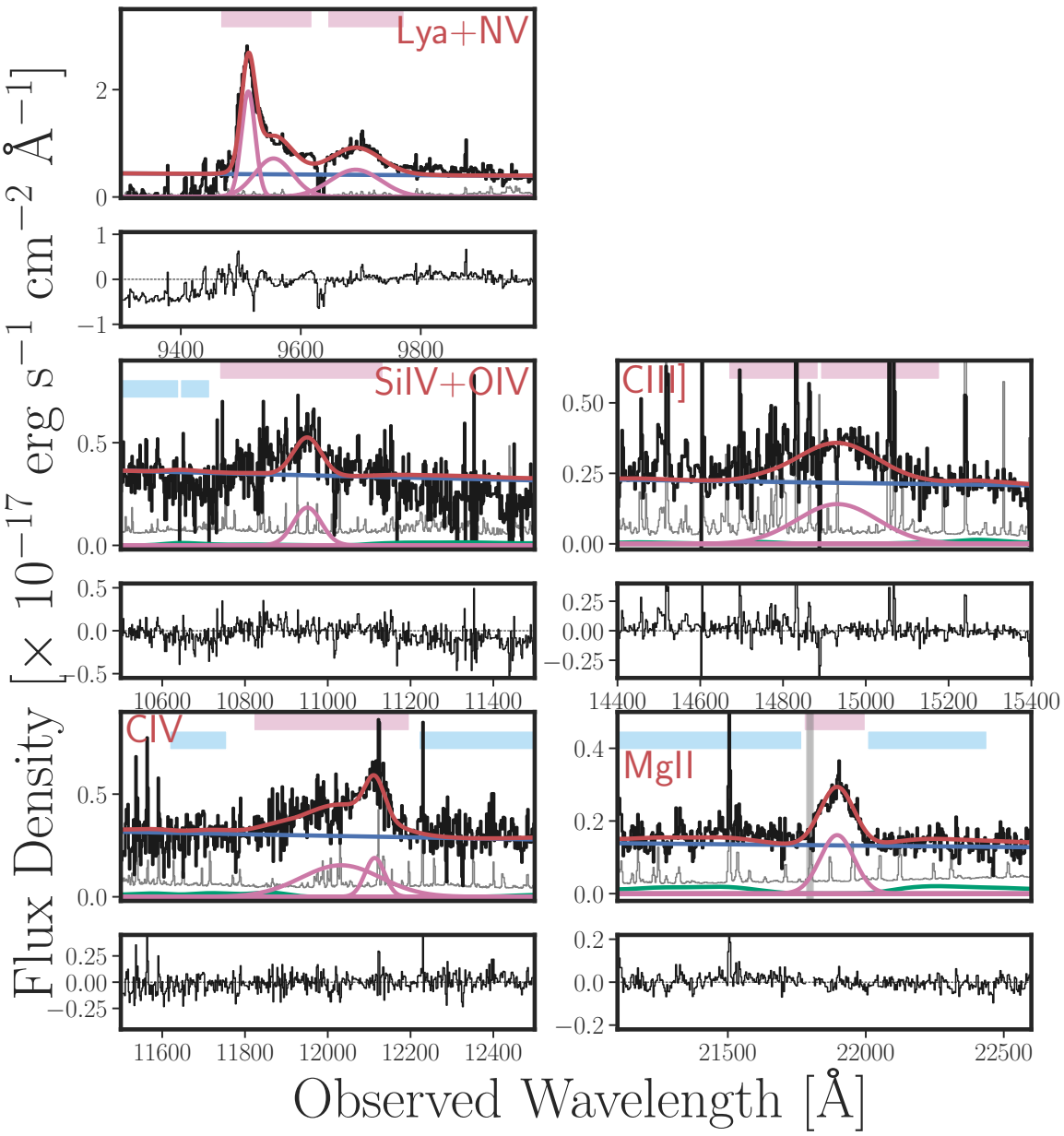

Figure 2. Zoom-in on the main broad emission lines from near-infrared spectroscopy. We show the total spectral fit (red line), and the different components, i.e. power law + Balmer pseudo-continuum (blue line), Fe II template (green line, from Vestergaard & Wilkes 2001), and emission lines (pink lines). Spectral regions used for the continuum and spectral line fits are shown as horizontal light blue and pink regions, respectively. The noise spectrum is reported in gray in the main panels, while residuals are also shown below each panel. Regions with low S/N or strong absorption features are masked out during the fit, and highlighted with gray vertical regions.

mon Astronomy Software Applications (CASA) package of the NRAO. The data were calibrated using the CASA pipeline version 5.4.1-23, and the continuum images were made using the wide-field w-projection gridder and Briggs weighting with robust=0.4 as implemented in the CASA task tclean. Due to the excision of data affected by RFI, the resulting L- and S-band images have the reference frequencies of 1.52 and 2.87 GHz, respectively. The resulting beam sizes for the 1.52 and 2.87 GHz images are $3\farcs55 \times 3\farcs24$ and $2\farcs27 \times 1\farcs85$, respectively. A summary of the radio observations is listed in Table 2 and the results are discussed in Sections 4.1 and 4.2. The follow-up radio images as well as archival data from the FIRST survey are shown in Figure 3.

3. ANALYSIS OF UV–OPTICAL PROPERTIES

To derive the properties of the broad emission lines, we use a tool especially designed to model near-infrared

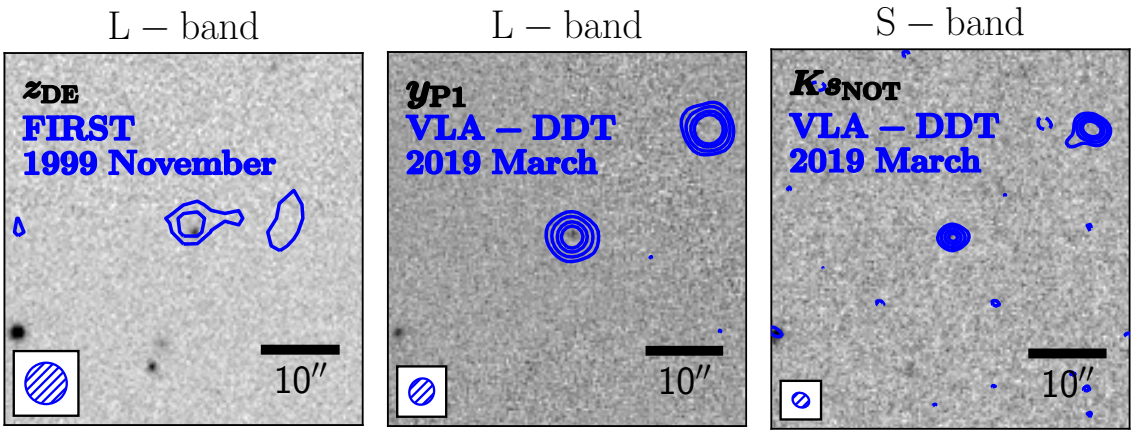

Figure 3. VLA L- and S-band observations (blue contours) centered on the position of P172+18 over optical and near-infrared imaging as labeled in the figure; north is up and east is left. Contours correspond to 3σ and 5σ for the FIRST image (left panel) and to 3σ, 7σ, 14σ, and 21σ for the VLA-DDT images (corresponding negative contours for all panels are dashed); σ for each of the radio images is listed in Table 2. The follow-up observations reveal a second radio source 23.″1 to the northwest of the quasar with no counterpart in available optical or near-infrared imaging (see Table 1). Although the secondary radio source is slightly brighter than the quasar in the deepest observations, it was not visible in the FIRST survey data.

spectra of high-redshift quasars, which is described in detail in Section 3 of Schindler et al. (2020). Briefly, we consider both the quasar pseudo-continuum emission and the broad emission lines. In particular, we fit the former with the following components:

1. a *power law* (f_{pl}), normalized at rest-frame wavelength 2500 Å:

$$f_{pl} = f_{pl,0} \left(\frac{\lambda}{2500\ \text{Å}} \right)^{\alpha_\lambda} \quad (1)$$

where α_λ and $f_{pl,0}$ are the power-law index and amplitude, respectively.

2. a *Balmer pseudo-continuum*. We consider the description from Dietrich et al. (2003), valid for wavelength $\lambda \leq \lambda_{\rm BE} = 3646$ Å, i.e., where the Balmer break occurs:

$$f_{BC}(\lambda) = f_{BC,0} B_\lambda(\lambda, T_e) \left(1 - e^{\tau_{\rm BE}(\lambda/\lambda_{\rm BE})^3} \right) \quad (2)$$

with $B_\lambda(T_e)$ the Planck function at electron temperature T_e, $\tau_{\rm BE}$ the optical depth at the Balmer edge, and $f_{BC,0}$ the normalized flux density at the Balmer break. Following the literature (e.g., Dietrich et al. 2003, Kurk et al. 2007, De Rosa et al. 2011, Mazzucchelli et al. 2017, Onoue et al. 2020), we assume $T_e = 15,000$ K and $\tau_{\rm BE} = 1$, and we fix the Balmer emission to 30% of the power-law contribution at rest-frame 3646 Å.

3. an *Fe II pseudo-continuum*. We model the Fe II contribution with the empirical template from Vestergaard & Wilkes (2001), which is used in the derivation of the scaling relation that we later consider for estimating the black hole mass of the quasar (see Section 3.2 and Equation 5). We fit the Fe II in the rest-frame wavelength range 1200 – 3500 Å. Assuming that Fe II emission arises from a region close to that responsible for the Mg II emission, we fix $z_{\rm FeII} = z_{\rm MgII}$ and $\text{FWHM}_{\rm FeII}$ to be equal to $\text{FWHM}_{\rm MgII}$.

To perform the fit, we choose regions of the quasar continuum free of broad emission lines and of strong spikes from residual atmospheric emission: [1336–1370], [1485–1503], [1562–1626], [2152–2266], [2526–2783], [2813–2869] Å (rest frame).

We subtract the entire pseudo-continuum model (power law + Fe II + Balmer pseudo-continuum) from the observed spectrum, and then we model the broad emission lines with Gaussian functions, interactively choosing the wavelength range for the fit. In particular, we model the N V, Si IV, C III], and Mg II lines with a single Gaussian, while the Lyα and C IV lines are better fit by two Gaussians representing a narrow component and a broad one.

After obtaining the best fit, we implement a second routine to obtain the best parameters and their uncertainties through a bootstrap resampling approach. The spectrum is resampled 500 times by drawing from a Gaussian distribution with mean and standard deviation equal to the observed spectrum and the uncertainty on each pixel, respectively. For every resampling, the spectrum is refit with the initial best fit used as a first guess. All the model parameters are then saved and used to build a distribution. The final best values and

uncertainties correspond to the 50% and 16% and 84% percentiles, respectively.

We show the total best fit of the final spectrum in Figure 1 and zoom-in on the emission lines in Figure 2. We list the measured quantities in Tables 1 and 4 and the derived properties in Table 5.

3.1. *Emission Line Properties*

Specific properties such as equivalent width (EW) and peak velocity shift of key broad emission lines (e.g., Lyα, N V, C IV, and Mg II) have been shown to trace properties of the innermost regions of quasars and of their accretion mechanisms (e.g, Leighly & Moore 2004, Richards et al. 2002, 2011).

We measure the redshifts of the emission lines as

$$z_{\rm line} = \frac{\lambda_{\rm line,obs}}{\lambda_{\rm line,rf}} - 1 \quad (3)$$

where $\lambda_{\rm line,obs}$ is the observed line wavelength, i.e., the peak of the fitted Gaussian function, and $\lambda_{\rm line,rf}$ is the rest-frame line wavelength (see Table 4). In case of a line fitted with two Gaussian functions (e.g., C IV and Lyα), we considered the peak wavelength corresponding to the maximum flux value of the full model (see Schindler et al. 2020 for further details).

P172+18 presents strong and narrow Lyα and N V emission lines (see Figures 1 and 2). We derive the total equivalent equivalent width of Lyα + N V, EW(Lyα + N V) $\sim$ 56 Å (see Table 4). This is consistent with the mean of the EW(Lyα + N V) distributions for $3 < z < 5$ and $z > 5.6$ quasars as found by Diamond-Stanic et al. (2009) and Bañados et al. (2016), respectively.

Notably for a $z \sim 7$ quasar, the narrow component of the Lyα emission of P172+18 can be fitted well by a single Gaussian and there is no evidence for an IGM Lyα damping wing (see Wang et al. 2020), implying that the surrounding IGM is > 90% ionized (see also Section 3.3).

Now we focus on the relation between the C IV EW and the blueshift with respect to the Mg II line. As a reminder, we model the C IV line with two Gaussians (see Table 4 and Figure 2). In the following, we consider all the components of the model, i.e., the total line emission[5]. We measure C IV EW $= 21.3^{+2.4}_{-2.0}$ Å and $\Delta v_{\rm MgII-CIV} = 195 \pm 225$ km s^{-1}. In Figure 4, we place the measurements of P172+18 in the context of quasar populations at $z \sim 2$ and $z \gtrsim 6$. For the $z \sim 2$ subsample we select quasars from the Sloan Digital Sky Survey (SDSS) Data Release 7 quasar catalog (DR7; Shen et al. 2011) using the criteria of Richards et al. (2011):

1. $1.54 < z < 2.2$, to ensure that both C IV and Mg II emission lines are encompassed by the SDSS spectral wavelength range.
2. FWHM$_{\rm CIV}$ and FWHM$_{\rm MgII}$ > 1000 km s^{-1}, to select only quasars with broad emission lines.
3. FWHM$_{\rm CIV}$ > $2\sigma_{\rm FWHM,CIV}$ and EW$_{\rm CIV}$ > $2\sigma_{\rm EW,CIV}$ and EW$_{\rm CIV}$ > 5 Å, for a reliable fit of the C IV line.
4. FWHM$_{\rm MgII}$ > $2\sigma_{\rm FWHM,MgII}$ and EW$_{\rm MgII}$ > $2\sigma_{\rm EW,MgII}$, for a reliable fit of the Mg II line.
5. we exclude broad absorption line quasars (`BAL_FLAG = 0`).

This yields 22,703 objects, out of which 1284 are classified as radio-loud with $R_{2500} > 10$.

As shown in Richards et al. (2011), radio-loud quasars occupy a specific region of the C IV EW–blueshift parameter space: small blueshifts ($\lesssim 1000$ km s^{-1}) but a wide range of EW values. However, note that for each radio-loud quasar several radio-quiet ones with similar rest-frame UV properties can be found, but not necessarily the other way around (Figure 4). Recently, the C IV emission line of $z \gtrsim 6$ quasars has been studied by various researchers (e.g., Mazzucchelli et al. 2017, Meyer et al. 2019). Large blue shifts for these objects are ubiquitous, with median values of $\Delta v_{\rm Mg\,II-C\,IV} \sim 1800$ km s^{-1} (Schindler et al. 2020) and with extreme values extending to $\Delta v_{\rm Mg\,II-C\,IV} \gtrsim 5000$ km s^{-1}(e.g., Onoue et al. 2020). In Figure 4 we show the $\Delta v_{\rm Mg\,II-C\,IV}$ measurements for $z > 6$ quasars from Mazzucchelli et al. (2017), Shen et al. (2019), Onoue et al. (2020), and Schindler et al. (2020).

To exclude objects with extremely faint emission lines and/or with spectra with low S/N close to the C IV line, we consider only high-z quasars for which EW$_{\rm CIV}$ > $2\sigma_{\rm CIV}$ and EW$_{\rm CIV}$ > 5 Å. Out of the three radio-loud quasars at $z > 6$ that have near-infrared spectra covering Mg II and C IV, only J1429+5447 does not satisfy our criteria owing to its extremely weak emission lines (EW$_{\rm CIV}$ < 5 Å; Shen et al. 2019). The two radio-loud quasars at $z > 6$ in Figure 4, J1427+3312 and P172+18, show C IV emission line properties consistent with what is observed in the radio-loud sample at $z \sim 2$. A larger sample of radio-loud quasars at high redshift with near-infrared spectra is needed to further investigate whether this trend changes with redshift, and whether the different EW and blueshift properties of radio-loud quasars can inform us about physical properties of their broad-line regions and/or their accretion mode.

[5] The properties of the single Gaussian components of the fit of the line are presented in Table 4

3.2. *Black Hole Properties*

We compute the quasar bolometric luminosity ($L_{\rm bol}$) using the bolometric correction presented by Richards et al. (2006):

$$L_{\rm bol} = 5.15\,\lambda\,L_{\lambda}(3000\,\text{Å})\,{\rm erg\,s^{-1}} \quad (4)$$

where $L_{\lambda}(3000\,\text{Å})$ is the monochromatic luminosity at 3000 Å derived from the power-law model. We estimate the black hole mass using the Mg II line as a proxy through the scaling relation presented by Vestergaard & Osmer (2009):

$$M_{\rm BH} = 10^{6.86}\left[\frac{\rm FWHM(MgII)}{10^{3}{\rm km\,s^{-1}}}\right]^{2}\left[\frac{\lambda L_{\lambda}(3000\,\text{Å})}{10^{44}{\rm erg\,s^{-1}}}\right]^{0.5} M_{\odot}. \quad (5)$$

This scaling relation has an intrinsic scatter of 0.55 dex, which is the dominant uncertainty of the black hole mass estimate. Once we have a black hole mass estimate, we can directly derive the Eddington luminosity as

$$L_{\rm Edd} = 1.3\times10^{38}\left(\frac{M_{\rm BH}}{M_{\odot}}\right){\rm erg\,s^{-1}}. \quad (6)$$

We obtain a black hole mass of $M_{\rm BH} = 2.9^{+0.7}_{-0.6}\times 10^{8} M_{\odot}$ and an Eddington ratio of $L_{\rm bol}/L_{\rm Edd} = 2.2^{+0.6}_{-0.4}$ for P172+18 (see also Table 5). We note that the Eddington ratio depends on the bolometric luminosity correction used. For example, using the correction recommended by Runnoe et al. (2012),

$$\log L_{\rm bol} = 1.852 + 0.975\times\log(\lambda\,L_{\lambda}(3000\,\text{Å})), \quad (7)$$

yields $L_{\rm bol} = 6.5\times10^{46}\,{\rm erg\,s^{-1}}$ and an Eddington ratio of $L_{\rm bol}/L_{\rm Edd} = 1.8$. For the reminder of the analysis we consider the bolometric correction from equation 4 to facilitate direct comparison with relevant literature (e.g., Shen et al. 2019; Schindler et al. 2020).

In Figure 5 we plot black hole mass vs. bolometric luminosity for P172+18 as well as other $z > 6$ and lower-redshift quasars from the literature. As for Figure 4, the low-redshift quasar sample is taken from the SDSS DR7 quasar catalog. Here, we select objects with redshift $0.35 < z < 2.25$, i.e., for which the Mg II emission line falls within the observed wavelength range, and with valid values of FWHM (Mg II) and $L_{\lambda}(3000)$, necessary to estimate the black hole masses and bolometric luminosities. This results in 85,504 SDSS quasars, out of which 5769 are classified as radio-loud (red contours in Figure 5). We compiled the $z > 6$ quasar sample from the following studies: Willott et al. (2010b), De Rosa et al. (2011), Wu et al. (2015), Mazzucchelli et al. (2017), Shen et al. (2019), Pons et al. (2019), Reed et al. (2019), Matsuoka et al. (2019b), Onoue et al. (2019, 2020), and Yang et al. (2020). We recalculate the black hole masses and bolometric luminosities of all quasars, at both low and high redshift using equations 4 and 5. The two high-redshift radio quasars for which these measurements are available from the literature (J1427+3312 and J1429+5447, both with near-infrared spectra presented by Shen et al. 2019), show black hole masses and bolometric luminosities consistent with radio-loud quasars at lower redshift, and with the general quasar population at $z > 6$. The black hole of P172+18 is accreting matter at a rate consistent with super-Eddington accretion, and it is found among the fastest accreting quasars at both $z \sim 1$ and $z \gtrsim 6$.

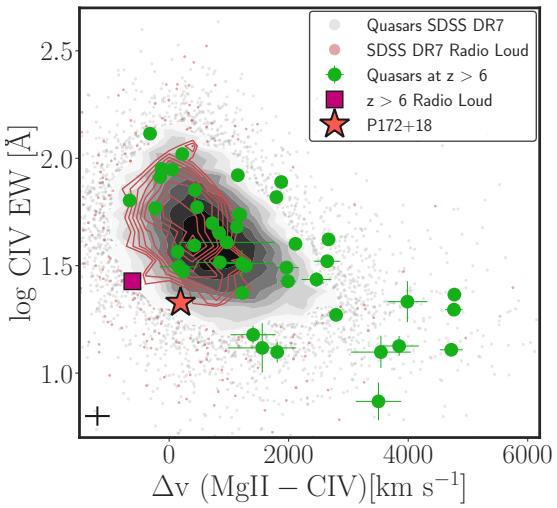

Figure 4. C IV equivalent width vs. blueshift with respect to the Mg II emission line. We show the distribution of SDSS DR7 $1.4 < z < 2.2$ quasars with gray points and shaded gray contours. The radio-loud subsample from SDSS is highlighted with red points and contours (see Section 3.1 for definition and selection). Quasars at $z > 6$ are reported with green points, and obtained from a collection of works from the literature (Mazzucchelli et al. 2017, Shen et al. 2019, Onoue et al. 2020, Schindler et al. 2020). Before this work, there was only one $z > 6$ radio-loud quasar with robust C IV and Mg II measurements (magenta square). P172+18 at $z = 6.823$ is represented as an orange star and its uncertainties are shown in the bottom left corner.

3.3. *Near-zone Size*

Near-zones are regions around quasars where the surrounding intergalactic gas has been ionized by the quasar's UV radiation, and they are observed as regions of enhanced transmitted flux close to the quasar in their rest-frame UV spectra. The near-zone sizes fo quasars provide constraints on quasar emission properties and on the state of their surrounding IGM (e.g., Fan et al.

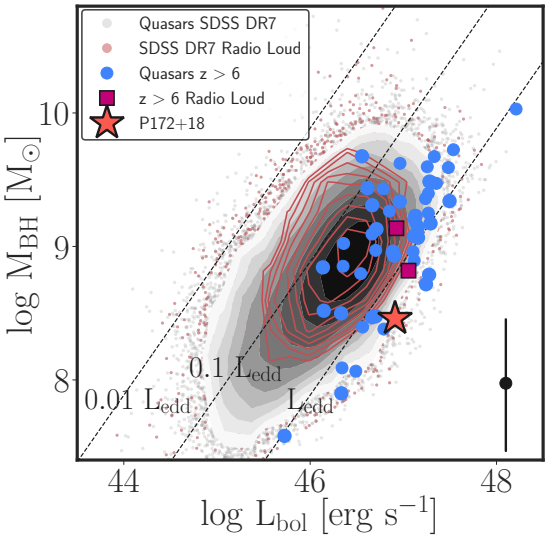

Figure 5. Black hole mass vs. bolometric luminosity. The gray points and contours show the distribution of SDSS DR7 quasars at $0.35 < z < 2.25$. Red points and contours highlight the SDSS DR7 radio-loud quasar subsample. We show $z > 6$ radio-quiet and radio-loud quasars from a collection of studies in the literature (see Section 3.2 for references) with blue circles and magenta squares, respectively. P172+18 (orange star) is consistent with accreting matter at super-Eddington rate. The dominant systematic uncertainty on black hole mass estimates from scaling relations (∼0.55 dex) is shown in the bottom right corner. All black hole masses shown here are estimated using the same scaling relation (Vestergaard & Osmer 2009), and the same bolometric correction was applied for all bolometric luminosities (Richards et al. 2006).

2006, Eilers et al. 2017, 2018). The radii of near-zones ($R_{\rm NZ}$) depend on the rate of ionizing flux from the central source, on the quasar's lifetime, and on the ionized fraction of the IGM (e.g., Fan et al. 2006, Davies et al. 2019). In practice, $R_{\rm NZ}$ is measured from the rest-frame UV spectrum (smoothed to a resolution of 20 Å) and taken to be the distance from the quasar at which the transmitted continuum-normalized flux drops below 10%. Here, we obtain the transmitted flux by dividing the observed spectrum of P172+18 by a model of the intrinsic continuum emission obtained with a principal components analysis method (see Davies et al. 2018; Eilers et al. 2020, for details of the method). In order to take into account the dependence on the quasar's luminosity, we also calculate the corrected near-zone radius ($R_{\rm NZ,corr}$), following the scaling relation presented by Eilers et al. (2017):

$$R_{\rm NZ,corr} = R_{\rm NZ} \times 10^{0.4(27+M_{1450})/2.35} \quad (8)$$

where M_{1450} is the absolute magnitude at rest-frame 1450 Å. We report both $R_{\rm NZ}$ and $R_{\rm NZ,corr}$ in Table 5.

The size of the near-zone of P172+18 and the corrected near-zone are $R_{\rm NZ} = 3.96 \pm 0.48$ pMpc and $R_{\rm NZ,corr} = 6.31 \pm 0.76$ pMpc, respectively. This large near-zone is within the top quintile of the distribution of quasar near-zones at $z \gtrsim 6$ (Eilers et al. 2017). This suggests that the time during which this quasar is UV-luminous (here referred to its lifetime) exceeds the average lifetime of the high-redshift quasar population of $t_{\rm Q} \sim 10^6$ yr (Eilers et al. 2020).

The evolution of $R_{\rm NZ,corr}$ with redshift, at $z > 5.5$, has been investigated in the literature to constrain both the reionization history and quasar lifetimes (e.g., Carilli et al. 2010, Davies et al. 2016, Eilers et al. 2020). While Carilli et al. (2010) and Venemans et al. (2015) recover a steep decline of $R_{\rm NZ,corr}$ with redshift (a decrease in size by a factor of ~ 6 between $z = 6$ and $z = 7$), Eilers et al. (2017) study a larger sample of ∼30 quasars at $5.8 < z < 6.6$ and recover a best-fit relation in the form of $R_{\rm NZ,corr} \propto (1+z)^{-\gamma}$, with $\gamma \sim 1.44$, suggesting a more moderate evolution with redshift than previous studies (a reduction in size by only ∼ 20% between $z = 6$ and $z = 7$). Finally, Mazzucchelli et al. (2017) recover a flatter relation ($\gamma \sim 1.0$), utilizing measurements of $R_{\rm NZ,corr}$ up to $z \sim 7$ (see also Ishimoto et al. 2020). Using hydrodynamical simulations, Chen & Gnedin (2020) obtained a shallow redshift evolution of near-zone sizes over the redshift range probed by the current quasar sample, i.e., $5.5 < z < 7$ (see also Davies et al. 2020). The expected average corrected near-zone size at $z = 6.8$ is $\langle R_{\rm NZ,corr} \rangle \approx 4.2$ pMpc for the redshift evolution from Eilers et al. (2017), and $\langle R_{\rm NZ,corr} \rangle \approx 2.2$ pMpc when assuming a steeper evolution as found by Venemans et al. (2015).

Therefore, the new near-zone measurement for P172+18 is considerably larger than the expected average size at this redshift. However, if the quasar was more luminous in the recent past and its activity is currently in a receding phase (see § 4.1 for tentative evidence of a decrease in the quasar's radio luminosity), the large near-zone size could be explained by a higher luminosity than what is measured at the present time.

4. ANALYSIS OF RADIO PROPERTIES

In addition to detecting the quasar, the follow-up VLA radio observations revealed a second radio source 23.″1 from P172+18 at a position angle of 128.25° (see Figure 3). We will explore the radio properties of the quasar and the serendipitous companion radio source below.

4.1. *Quasar Radio Properties*

The quasar is a point source in both the follow-up L- and S-band observations with a deconvolved size smaller

Table 1. Photometry of the radio-loud quasar P172+18 and its radio companion.

	Quasar	Radio Companion
R.A. (J2000)	$11^{\rm h}29^{\rm m}25\overset{\rm s}{.}37$	$11^{\rm h}29^{\rm m}24\overset{\rm s}{.}08$
Decl. (J2000)	$+18°46'24\overset{''}{.}29$	$+18°46'38\overset{''}{.}58$
Public optical and infrared surveys		
Pan-STARRS1 $i_{\rm P1}$	> 23.6	> 23.6
Pan-STARRS1 $z_{\rm P1}$	> 23.2	> 23.2
Pan-STARRS1 $y_{\rm P1}$	20.76 ± 0.09	> 22.3
DECaLS DR8 $g_{\rm DE}$	> 25.4	> 25.4
DECaLS DR8 $r_{\rm DE}$	> 24.8	> 24.8
DECaLS DR8 $z_{\rm DE}$	21.64 ± 0.05	> 23.8
DECaLS DR8 $W1$	20.71 ± 0.13	> 21.8
DECaLS DR8 $W2$	20.73 ± 0.31	> 20.9
Follow-up near-infrared imaging		
$J_{\rm NOT}$	20.90 ± 0.11	> 22.2
$H_{\rm NOT}$	21.36 ± 0.24	> 21.8
$Ks_{\rm NOT}$	21.07 ± 0.18	> 21.7
Public radio surveys		
TGSS 147.5 MHz	< 8.5 mJy	< 8.5 mJy
FIRST 1.4 GHz	$1020 \pm 144\,\mu$Jy[a]	$< 406\,\mu$Jy
Radio follow-up		
VLA-L 1.52 GHz	$510 \pm 15\,\mu$Jy	$732 \pm 15\,\mu$Jy
VLA-S 2.87 GHz	$222 \pm 9\,\mu$Jy	$432 \pm 20\,\mu$Jy[b]
α_S^L	-1.31 ± 0.08	-0.83 ± 0.08
Quasar rest-frame luminosities[c]		
m_{1450}	21.08 ± 0.10	
M_{1450}	-25.81 ± 0.10	
L_{2500}	$(1.4 \pm 0.1) \times 10^{46}$ erg s^{-1}	
L_{3000}	$(1.3 \pm 0.1) \times 10^{46}$ erg s^{-1}	
L_{4400}	$(1.1 \pm 0.1) \times 10^{46}$ erg s^{-1}	
$L_{5\,\rm GHz}$	$(5.4 \pm 0.2) \times 10^{42}$ erg s^{-1}	

[a] This is the reported peak flux density in the FIRST catalog (version 2014dec17). We note that in the FIRST image we measure $852 \pm 135\,\mu$Jy.

[b] The source is marginally resolved in the VLA-S image and we report the integrated flux.

[c] The quasar UV and optical luminosities are derived from the best-fit power law of the near-infrared spectrum (see Table 4) and the uncertainties are dominated by the $J_{\rm NOT}$ photometry used for absolute flux calibration of the spectrum. The 5 GHz radio luminosity is extrapolated using the measured radio index.

than $1\overset{''}{.}9 \times 0\overset{''}{.}87$; see Figure 3. P172+18 is well detected in both bands with S/N > 20 and the measured flux densities are listed in Table 1. The measured L-band flux density is a factor of two fainter than what is reported in the FIRST catalog. In fact, the measured $f_{1.52\,\rm GHz} = 510 \pm 15\,\mu$Jy would have been below the detection threshold of the FIRST survey (Becker et al. 1995). The discrepancy is significant at more than 3σ and could be the result of real quasar variability over the 20 yr ($\sim$ 2.5 yr rest frame) between the two measurements; such changes have been reported in similar timescales (e.g., Nyland et al. 2020). However, given that the source is at the faint limit of the FIRST survey, we cannot rule out that the variation is simply due to noise fluctuations in the FIRST data. Unfortunately, we are not able to test the variability hypothesis given that no other measurements of the quasar are available at a similar epoch to the FIRST observation. For the remainder of the analysis we will consider the follow-up VLA measurements as the true fluxes. Assuming that the radio observations follow a power-law spectral energy distribution ($f_\nu \propto \nu^\alpha$), the L- and S-band flux densities correspond to a steep power-law radio slope of $\alpha_S^L = -1.31 \pm 0.08$. This is steeper than $\alpha = -0.75$, which is usually assumed in high-redshift quasar studies when only one radio band is available (e.g., Wang et al. 2007; Momjian et al. 2014; Bañados et al. 2015).

4.1.1. *Radio-loudness*

To estimate the radio-loudness of P172+18 we obtain the rest-frame 5 GHz emission by extrapolating the radio emission using the measured spectral index $\alpha_S^L = -1.31$ and the 2500 Å and 4400 Å emission using the power-law fit to the near-infrared spectrum ($\alpha_{\nu,\rm UV} = -0.48$) obtained in Section 3. This results in radio-loudness parameters of $R_{2500} = 91 \pm 9$ and $R_{4400} = 70 \pm 7$, classifying P172+18 as a radio-loud quasar. The quasar radio properties are summarized in Table 5.

We note that the data from very long baseline interferometry (VLBI) presented by Momjian et al. (2021) imply a steeper spectral index at frequencies higher than 3 GHz (see Figure 6). The quasar is not detected in the TIFR GMRT Sky Survey (TGSS; Intema et al. 2017) at 147.5 MHz. We downloaded the TGSS image and determined a 3σ upper limit of 8.5 mJy (see Table 1 and Figure 6). This implies that the slope of the radio spectrum should flatten or have a turnover between 147.5 MHz and 1.52 GHz. If the turnover occurs at a frequency larger than rest-frame 5 GHz, the rest-frame 5 GHz luminosity (and therefore radio-loudness) would be smaller than our fiducial value assuming $\alpha = -1.31$. In the extreme case that the turnover happened exactly at the frequency of our L-band observations, the source would still be classified as radio-loud (i.e., $R_{2500} > 10$) as long as $\alpha < 1.24$ (see Figure 6). Deep radio observations at frequencies < 1 GHz are needed to precisely determine the rest-frame 5 GHz luminosity and the shape of the radio spectrum.

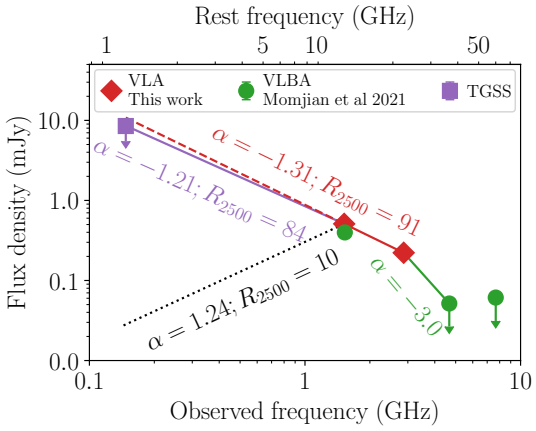

Figure 6. Radio spectral energy distribution of P172+18, including data from our VLA follow-up observations (red diamond), the VLBI measurements (green circles) from Momjian et al. (2021), and a 3σ upper limit from the TGSS (purple square). The power-law index, α, is shown between the measurements as well as the radio-loudness by extrapolating the radio emission to rest-frame 5GHz. The dotted line with $\alpha = 1.24$ represents the turnover required for P172+18 to be classified as radio-quiet (i.e., $R_{2500} < 10$).

4.2. *Companion Radio Source*

The radio companion is detected with S/N > 20 in both L- and S-band observations (see Figure 3). This object is a point source in the L-band image with a deconvolved size smaller than $1\farcs6 \times 0\farcs69$. A Gaussian fit to the S-band image results in a resolved source with a deconvolved size of $1\farcs3 \times 0\farcs8$ and position angle of $74^\circ \pm 22^\circ$. This secondary source is not detected in any of our available optical, near-infrared, and mid-infrared images. Its radio properties and optical/near-infrared limits are listed in Table 1.

The number of radio sources with a 1.4 GHz flux density $> 700\,\mu$Jy is $59\,\mathrm{deg}^{-2}$ and $117\,\mathrm{deg}^{-2}$ according to the number counts of deep radio surveys from Fomalont et al. (2006) and Bondi et al. (2008), respectively. This means that in an area encompassing the quasar and the second radio source ($\pi \times 23\farcs1^2$) only 0.007 and 0.015 sources like the companion are expected using the number counts from Fomalont et al. (2006) and Bondi et al. (2008), respectively. The $< 2\%$ likelihood of chance superposition raises the possibility that this radio source and the quasar could be associated.

This companion radio source is (slightly) brighter than the quasar in both the L- and S-band follow-up observations. However, it was not detected in the FIRST survey carried out in 1999 (see Table 1 and Figure 3). This second source could not be a hot spot of the radio jet expanding for the last 20 yr: at the redshift of the quasar, the projected separation of the two sources is about 120 proper kpc, a distance that would take light about 400,000 yr to travel.

Another possibility is that this second source is an obscured, radio-AGN companion. There are a few examples of associated dust-obscured, star-forming companion galaxies to quasars at $z > 6$ (e.g., Decarli et al. 2017; Neeleman et al. 2019). A couple of them have tentative X-ray detections, which make them obscured AGN candidates (e.g., Connor et al. 2019; Vito et al. 2019). This possibility is tempting, because two associated radio-loud AGNs would point to an overdense environment in the early universe and provide constraints on AGN clustering. Nevertheless, with the available shallow optical and near-infrared data we are not able to rule out that the second radio source lies at a different redshift than that of the quasar. More follow-up observations are required to firmly establish the nature and redshift of the source.

5. SUMMARY AND CONCLUSIONS

The main results of this work can be summarized as follows.

1. We present the discovery of the most distant radio-loud source to date, the quasar P172+18 with an Mg II-based redshift of $z = 6.823$ (see Figures 1 and 7 and Table 5).

2. The C IV properties of the two $z > 6$ radio-loud quasars known with near-infrared spectroscopy and reliable C IV detection (J1427+5447 and P172+18) are consistent with the radio-loud population at $z \sim 2$ in terms of C IV EW and blueshift (see Figure 4).

3. The quasar has a black hole mass of $\sim 2.9 \times 10^8 M_\odot$ and an Eddington ratio of ~2.2. It is known that there are large uncertainties on the estimates of black hole mass and Eddington ratio associated with the scaling relations used. Therefore we compare the properties of P172+18 to other quasars using the same scaling relation (Vestergaard & Osmer 2009) and bolometric correction (Richards et al. 2006). With this in mind, P172+18 is among the fastest accreting quasars at both low and high redshift (Figure 5).

4. The quasar shows a strong Lyα line that can be modeled with a narrow Gaussian and a broad one (see Figure 2 and Table 3). The large measured near-zone size, $R_{\mathrm{NZ,corr}} \sim 6$ pMpc, suggests an ionized IGM around the quasar and implies that P172+18's lifetime exceeds the average lifetime of the $z \gtrsim 6$ quasar population (see Section 3.3).

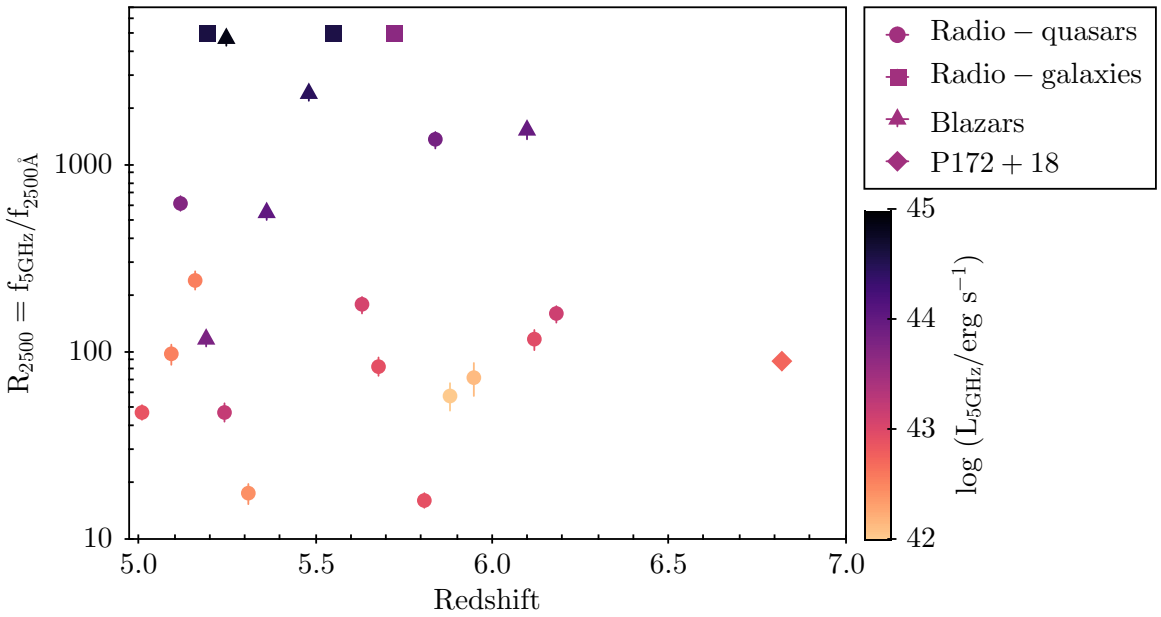

Figure 7. All radio-loud ($R_{2500} > 10$) sources known at $z > 5$, color-coded by their rest-frame 5 GHz radio luminosity. Radio-loud quasars are shown as circles and radio galaxies as squares. The radio-loudness for radio galaxies has been fixed to 5000 for visualization purposes. The properties and references for all these sources are listed in Table 6.

5. The quasar's radio emission is unresolved (with size smaller than $1\farcs90 \times 0\farcs87$) and shows a steep radio spectrum ($\alpha = -1.31 \pm 0.08$) between 1.5 and 3.0 GHz (∼11–23 GHz in the rest frame). Extrapolating the spectrum to 5 GHz rest frame, the quasar has a radio-loudness of $R_{2500} = 91 \pm 9$ (see Figure 6).

6. The follow-up L-band radio data are a factor ∼ 2 fainter than what is expected from the FIRST observations taken two decades previously. This fact, together with the long lifetime implied by the size of P172+18's near-zone, could indicate that we are witnessing the quasar phase turning off.

7. The VLA follow-up observations revealed a second radio source $23\farcs1$ from the quasar with comparable radio flux densities (see Figure 3 and Table 1). This source was not detected in the FIRST survey and has no counterpart in our current optical/near-infrared images.

P172+18, in particular, is an ideal target to investigate the existence of extended X-ray emission arising from the interaction between relativistic particles in radio jets and a hot cosmic microwave background (CMB) (e.g., Wu et al. 2017). This effect is expected to be particularly strong at the highest redshifts because the CMB energy density scales as $(1 + z)^4$ and as a result its effective magnetic field can be stronger than the one in radio-lobes (Ghisellini et al. 2015). Complementary to this science case will be high-resolution VLBI observations to constrain the structure of the radio emission (e.g., Frey et al. 2008; Momjian et al. 2008, 2018). VLBI observations for P172+18 already exist and the results will be presented in the companion paper by Momjian et al. (2021).

The serendipitous detection of the companion radio source (see Figure 3) deserves further follow-up. If the radio source lies at the same redshift as the quasar, this could be the most distant AGN pair known, potentially revealing a very dense region in the early universe. Telescopes such as the Atacama Large Millimeter/submillimeter Array or the James Webb Space Telescope should be able to determine the exact redshift by identifying far-infrared and optical emission lines from this possible obscured AGN.

Out of the 18 quasars known at $z > 6.8$, P172+18 is the only one currently classified as radio-loud. In Table 6 we compile the information on all the radio-loud sources at $z > 5$ known to date and in Figure 7 we present their redshift and radio-loudness distribution. The radio-loudness of P172+18 is consistent with the median value of the $z > 5$ radio-loud quasar population ($R_{2500,\mathrm{median}} = 91$; $R_{2500,\mathrm{mean}} = 213$). Thus, the existence of this "median" radio-loud quasar at $z = 6.823$ makes it likely that there are other radio-loud sources waiting to be discovered (or categorized) between this redshift and the previous redshift record, and possibly even at $z > 7$. Identifying these radio sources would be important for future 21cm absorption studies of the

IGM with the Square Kilometre Array (Carilli et al. 2004; Carilli & Rawlings 2004; Ciardi et al. 2015).

ACKNOWLEDGMENTS

E.B. thanks Aaron Meisner and Eddie Schlafly for helpful discussions about DECaLS and unWISE data. E.B. thanks Sofía Rojas and Yana Khusanova for useful feedback on a previous version of this manuscript. E.B. is extremely grateful to all the staff at Las Campanas Observatory for making all observing runs an unforgettable experience.

C.M. acknowledges Eleonora Sani for useful discussion on quasar spectral fitting.

Research by A.J.B. is supported by NSF grant AST-1907290.

A.C.E. acknowledges support by NASA through the NASA Hubble Fellowship grant #HF2-51434 awarded by the Space Telescope Science Institute, which is operated by the Association of Universities for Research in Astronomy, Inc., for NASA, under contract NAS5-26555.

The work of T.C. and D.S. was carried out at the Jet Propulsion Laboratory, California Institute of Technology, under a contract with NASA. T.C.'s research was supported by an appointment to the NASA Postdoctoral Program at the Jet Propulsion Laboratory, California Institute of Technology, administered by Universities Space Research Association under contract with NASA.

B.P.V. acknowledges funding through the ERC Advanced Grant 740246 (Cosmic Gas).

We are grateful to the ESO and VLA staff for providing DDT observations for this program.

The National Radio Astronomy Observatory is a facility of the National Science Foundation operated under cooperative agreement by Associated Universities, Inc.

This work is based on observations collected at the European Southern Observatory under ESO program 2102.A-5042(A). This paper includes data gathered with the 6.5 m Magellan Telescopes located at Las Campanas Observatory, Chile.

This paper includes data from the LBT. The LBT is an international collaboration among institutions in the United States, Italy, and Germany. The LBT Corporation partners are: The University of Arizona on behalf of the Arizona university system; Istituto Nazionale di Astrofisica, Italy; LBT Beteiligungsgesellschaft, Germany, representing the Max Planck Society, the Astrophysical Institute Potsdam, and Heidelberg University; The Ohio State University; The Research Corporation, on behalf of The University of Notre Dame, University of Minnesota and University of Virginia.

Some of the data presented in this paper were obtained at the W.M. Keck Observatory, which is operated as a scientific partnership among the California Institute of Technology, the University of California and the National Aeronautics and Space Administration. The Observatory was made possible by the generous financial support of the W.M. Keck Foundation. Keck data presented herein were obtained using the UCI Remote Observing Facility, made possible by a generous gift from John and Ruth Ann Evans.

The authors wish to recognize and acknowledge the very significant cultural role and reverence that the summit of Maunakea has always had within the indigenous Hawaiian community. We are most fortunate to have the opportunity to conduct observations from this mountain.

Based on observations made with the Nordic Optical Telescope, operated by the Nordic Optical Telescope Scientific Association at the Observatorio del Roque de los Muchachos, La Palma, Spain, of the Instituto de Astrofisica de Canarias.

Facilities: EVLA, Keck:II (NIRES), VLT:Kueyen (X-Shooter), Magellan:Baade (FIRE), LBT (MODS), NOT (NOTCam).

Software: Astropy (Astropy Collaboration et al. 2018), CASA (McMullin et al. 2007), Matplotlib (Hunter 2007, http://www.matplotlib.org), Numpy (Harris et al. 2020), PypeIt (Prochaska et al. 2019; Prochaska et al. 2020), SciPy (Virtanen et al. 2020), TOPCAT (Taylor 2005, http://www.starlink.ac.uk/topcat/)

REFERENCES

An, H., & Romani, R. W. 2018, ApJ, 856, 105, doi: 10.3847/1538-4357/aab435

Andika, I. T., Jahnke, K., Onoue, M., et al. 2020, ApJ, 903, 34, doi: 10.3847/1538-4357/abb9a6

Astropy Collaboration, Price-Whelan, A. M., Sipőcz, B. M., et al. 2018, AJ, 156, 123, doi: 10.3847/1538-3881/aabc4f

Bañados, E., Carilli, C., Walter, F., et al. 2018a, ApJL, 861, L14, doi: 10.3847/2041-8213/aac511

Bañados, E., Venemans, B. P., Morganson, E., et al. 2014, AJ, 148, 14, doi: 10.1088/0004-6256/148/1/14

—. 2015, ApJ, 804, 118, doi: 10.1088/0004-637X/804/2/118

Table 2. Observing Log of Optical and Radio Imaging

Date	Telescope/Instrument	Filters/frequency	rms (1σ)	Reference
2019 May 17	NOT/NOTCAM	$J_{\rm NOT}$,$H_{\rm NOT}$	23.4, 23.0 mag	This work
2019 May 18	NOT/NOTCAM	$Ks_{\rm NOT}$	22.9 mag	This work
1999 Nov 10	VLA/L-band	1.44 GHz	135 μJy	FIRST
2019 Mar 5	VLA/S-band	2.87 GHz	9 μJy	This work
2019 Mar 11	VLA/L-band	1.58 GHz	15 μJy	This work

Table 3. Summary of the optical and near-infrared follow-up spectroscopic observations.

Date	Telescope/Instrument	Exposure Time	Wavelength Range	Slit Width
2019 Feb 18	Keck/NIRES	3.5 hr	9400−24000 Å	0.″55
2019 Mar 8−Apr 8	VLT/X-Shooter	3.5 hr	3000−24800 Å	1.″0 / 0.″9 / 0.″6
2019 Jun 13	LBT/MODS	0.3 hr	5000−10000 Å	1.″22

Table 4. Properties of P172+18 measured from near-infrared spectroscopy.

Emission Line	Redshift	FWHM (km s^{-1})	EW (Å)	$\Delta v_{\rm MgII-line}$ (km s^{-1})
Lyα (1)	6.8234±0.0002	891^{+27}_{-25}	–	−15±77
Lyα (2)	6.854±0.001	2870^{+91}_{-77}	–	−304±88
Lyα [a]	6.8246±0.0008	1103^{+27}_{-22}	38.1±1.8	−60±83
N V	6.817±0.001	$3076^{+0.3}_{-0.1}$	18.1±1.1	215±91
Lyα + N V	–	–	56.3±3.0	–
Si IV+ [O IV]	6.822±0.05	3044^{+1104}_{-652}	$8.6^{+1.7}_{-1.4}$	38±1918
C IV (1)	$6.819^{+0.004}_{-0.007}$	1699^{+840}_{-499}	–	153±224
C IV (2)	$6.753^{+0.02}_{-0.03}$	5001^{+1018}_{-2143}	–	2682±961
C IV [a]	$6.818^{+0.004}_{-0.006}$	2714^{+1704}_{-945}	$21.3^{+2.4}_{-2.0}$	192±225
C III]	$6.799^{+0.008}_{-0.005}$	5073^{+560}_{-461}	$28.9^{+3.4}_{-3.3}$	920±260
Mg II [b]	$6.823^{+0.003}_{-0.001}$	1780^{+100}_{-50}	$20.8^{+2.8}_{-2.6}$	–
Power-law slope ($\alpha_{\lambda,\rm UV}$)	–1.52 ± 0.05			
Power-law ampl. ($f_{\lambda,2500,\rm obs}$)	1.36 ± 0.03 [$\times$ 10^{-18} erg s^{-1} cm^{-2} Å^{-1}]			

Bañados, E., Venemans, B. P., Decarli, R., et al. 2016, ApJS, 227, 11, doi: 10.3847/0067-0049/227/1/11

Bañados, E., Venemans, B. P., Mazzucchelli, C., et al. 2018b, Nature, 553, 473, doi: 10.1038/nature25180

Becker, R. H., White, R. L., & Helfand, D. J. 1995, ApJ, 450, 559, doi: 10.1086/176166

Belladitta, S., Moretti, A., Caccianiga, A., et al. 2020, A&A, 635, L7, doi: 10.1051/0004-6361/201937395

Bondi, M., Ciliegi, P., Schinnerer, E., et al. 2008, ApJ, 681, 1129, doi: 10.1086/589324

Carilli, C. L., Furlanetto, S., Briggs, F., et al. 2004, NewAR, 48, 1029, doi: 10.1016/j.newar.2004.09.046

Carilli, C. L., Gnedin, N. Y., & Owen, F. 2002, ApJ, 577, 22, doi: 10.1086/342179

Carilli, C. L., & Rawlings, S. 2004, NewAR, 48, 979, doi: 10.1016/j.newar.2004.09.001

Table 5. P172+18 properties derived from the optical and near-infrared spectroscopy and radio observations.

Quantity	
$L_{\rm bol}$	$(8.1 \pm 0.3) \times 10^{46}$ erg s^{-1}
$M_{\rm BH}$	$2.9^{+0.7}_{-0.6} \times 10^8$ $M_\odot$
$L_{\rm bol}/L_{\rm Edd}$	$2.2^{+0.6}_{-0.4}$
Fe II/Mg II	2.8±1.0
$R_{\rm NZ}$	3.96 ± 0.48 pMpc
$R_{\rm NZ,corr}$	6.31 ± 0.76 pMpc
R_{2500}	91 ± 9
R_{4400}	70 ± 7

Carilli, C. L., Wang, R., Fan, X., et al. 2010, ApJ, 714, 834, doi: 10.1088/0004-637X/714/1/834

Chambers, K. C., Magnier, E. A., Metcalfe, N., et al. 2016, ArXiv e-prints. https://arxiv.org/abs/1612.05560

Chen, H., & Gnedin, N. Y. 2020, arXiv e-prints, arXiv:2008.04911. https://arxiv.org/abs/2008.04911

Ciardi, B., Inoue, S., Mack, K., Xu, Y., & Bernardi, G. 2015, in Advancing Astrophysics with the Square Kilometre Array (AASKA14), 6. https://arxiv.org/abs/1501.04425

Ciardi, B., Labropoulos, P., Maselli, A., et al. 2013, MNRAS, 428, 1755, doi: 10.1093/mnras/sts156

Clough, S. A., Shephard, M. W., Mlawer, E. J., et al. 2005, JQSRT, 91, 233, doi: 10.1016/j.jqsrt.2004.05.058

Condon, J. J., Cotton, W. D., Greisen, E. W., et al. 1998, AJ, 115, 1693, doi: 10.1086/300337

Connor, T., Bañados, E., Stern, D., et al. 2019, ApJ, 887, 171, doi: 10.3847/1538-4357/ab5585

Cutri, R. M., e. 2014, VizieR Online Data Catalog, 2328, 0

Davies, F. B., Furlanetto, S. R., & McQuinn, M. 2016, MNRAS, 457, 3006, doi: 10.1093/mnras/stw055

Davies, F. B., Hennawi, J. F., & Eilers, A.-C. 2019, ApJL, 884, L19, doi: 10.3847/2041-8213/ab42e3

—. 2020, MNRAS, 493, 1330, doi: 10.1093/mnras/stz3303

Davies, F. B., Hennawi, J. F., Bañados, E., et al. 2018, ApJ, 864, 143, doi: 10.3847/1538-4357/aad7f8

De Rosa, G., Decarli, R., Walter, F., et al. 2011, ApJ, 739, 56, doi: 10.1088/0004-637X/739/2/56

Decarli, R., Walter, F., Venemans, B. P., et al. 2017, Nature, 545, 457, doi: 10.1038/nature22358

Dey, A., Schlegel, D. J., Lang, D., et al. 2019, AJ, 157, 168, doi: 10.3847/1538-3881/ab089d

Diamond-Stanic, A. M., Fan, X., Brandt, W. N., et al. 2009, ApJ, 699, 782, doi: 10.1088/0004-637X/699/1/782

Dietrich, M., Hamann, F., Appenzeller, I., & Vestergaard, M. 2003, ApJ, 596, 817, doi: 10.1086/378045

Djupvik, A. A., & Andersen, J. 2010, Astrophysics and Space Science Proceedings, 14, 211, doi: 10.1007/978-3-642-11250-8_21

Drouart, G., Seymour, N., Galvin, T. J., et al. 2020, PASA, 37, e026, doi: 10.1017/pasa.2020.6

Eilers, A.-C., Davies, F. B., & Hennawi, J. F. 2018, ApJ, 864, 53, doi: 10.3847/1538-4357/aad4fd

Eilers, A.-C., Davies, F. B., Hennawi, J. F., et al. 2017, ApJ, 840, 24, doi: 10.3847/1538-4357/aa6c60

Eilers, A.-C., Hennawi, J. F., Decarli, R., et al. 2020, ApJ, 900, 37, doi: 10.3847/1538-4357/aba52e

Eisenhardt, P. R. M., Marocco, F., Fowler, J. W., et al. 2020, ApJS, 247, 69, doi: 10.3847/1538-4365/ab7f2a

Fan, X., Narayanan, V. K., Lupton, R. H., et al. 2001, AJ, 122, 2833, doi: 10.1086/324111

Fan, X., Strauss, M. A., Richards, G. T., et al. 2006, AJ, 131, 1203, doi: 10.1086/500296

Fomalont, E. B., Kellermann, K. I., Cowie, L. L., et al. 2006, ApJS, 167, 103, doi: 10.1086/508169

Frey, S., Gurvits, L. I., Paragi, Z., & É. Gabányi, K. 2008, A&A, 484, L39, doi: 10.1051/0004-6361:200810040

Frey, S., Paragi, Z., Fogasy, J. O., & Gurvits, L. I. 2015, MNRAS, 446, 2921, doi: 10.1093/mnras/stu2294

Ghisellini, G., Haardt, F., Ciardi, B., et al. 2015, MNRAS, 452, 3457, doi: 10.1093/mnras/stv1541

Gullikson, K., Dodson-Robinson, S., & Kraus, A. 2014, AJ, 148, 53, doi: 10.1088/0004-6256/148/3/53

Hardcastle, M. J., & Croston, J. H. 2020, NewAR, 88, 101539, doi: 10.1016/j.newar.2020.101539

Harris, C. R., Millman, K. J., van der Walt, S. J., et al. 2020, Nature, 585, 357, doi: 10.1038/s41586-020-2649-2

Table 6. Census and Properties of $z > 5$ Radio-loud Sources, Sorted by Decreasing Redshift, z

Name	z	Type	m_{1450} [a]	$\alpha_{\lambda,\rm UV}$ [b]	$f_{1.4\,\rm GHz}$	$\alpha_{\nu,\rm radio}$	R_{2500} [c]	References
			(mag)		(mJy)			disc./z/m_{1450}/$\alpha_{\lambda,\rm UV}$/$f_{1.4\,\rm GHz}$/$\alpha_{\nu,\rm radio}$
P172+18	6.823	quasar	21.08	−1.52	0.510 ± 0.016	−1.31	91 ± 9	1/1/1/1/1/1
J1429+5447	6.183	quasar	20.70	−1.22	2.93 ± 0.15	−0.67	161 ± 17	2/3/4/–/5/6
J1427+3312	6.121	quasar	20.68	–	1.73 ± 0.13	−0.90	117 ± 14	7,8/9/4/–/5/6
J0309+27172	6.10	blazar	20.96	–	23.89 ± 0.87	−0.44	1521 ± 151	10/10/11/–/12/10
J2228+0110	5.95	quasar	22.20	–	0.31 ± 0.06	–	71 ± 15	13/13/13/–/13/–
J2242+0334	5.88	quasar	22.20	–	0.20 ± 0.03	−1.06	58 ± 9	2/2/4/–/14/14
P352–15	5.84	quasar	21.05	–	14.9 ± 0.70	−0.89	1358 ± 141	15/15/15/–/12/15
J0836+0054	5.81	quasar	18.95	−0.73	1.74 ± 0.04	−0.86	16 ± 1	16/17/4/9/18/6
J1530+1049	5.72	radio galaxy	–	–	7.50 ± 0.10	−1.40	–	19/19/–/–/19/19
P055–00	5.68	quasar	20.29	–	2.14 ± 0.14	–	83 ± 9	20/20/4/–/5/–
P135+16	5.63	quasar	20.74	–	3.04 ± 0.15	–	177 ± 18	20/20/4/–/5/–
J0856+0223	5.55	radio galaxy	–	–	86.50 ± 0.60	−0.89	–	21/21/–/–/21/21
J0906+6930	5.48	blazar	19.67	−2.00	92.0 ± 0.62	−0.40	2373 ± 205	22/23/11/23/22/22
J1648+4603	5.36	blazar	19.51	–	34.0 ± 0.01	−0.47	552 ± 47	24/24/11/–/24/24
J1614+4650	5.31	quasar	19.72	–	1.69 ± 0.16	0.67	17 ± 2	24/25/11/–/5/6
J1026+2542	5.25	blazar	19.69	–	230.00 ± 0.14	−0.60	4701 ± 407	24/25/11/–/5/26
J2329+3003	5.24	quasar	18.83	–	4.90 ± 0.40	–	47 ± 5	27/28/27/–/12/–
J0924–2201	5.19	radio galaxy	–	–	71.10 ± 0.10	−1.63	–	29/29/–/–/29/29
J0131–0321	5.189	blazar	18.09	−1.75	32.83 ± 0.12	0.29	116 ± 9	30/30/30/30/5/6
J2245+0024	5.16	quasar	22.24	–	1.09 ± 0.06	–	240 ± 27	31/31/31/–/32/–
J0913+5919	5.12	quasar	20.26	–	17.45 ± 0.16	−0.67	618 ± 55	24/25/11/–/5/33
J2239+0030	5.09	quasar	21.27	–	1.35 ± 0.10	−0.27	98 ± 12	31/31/31/–/5/6
J1034+2033	5.01	quasar	19.56	–	3.96 ± 0.15	0.28	47 ± 4	24/25/11/–/5/6

[a] For objects for which the rest-frame 1450 Å magnitudes are not reported in the literature or have large uncertainties, we use as proxy their $y_{\rm P1}$ magnitude from Pan-STARRS1 (Reference 11).

[b] We report rest-frame UV power-law slopes for objects with available near-infrared spectra covering at least from 1 μm to 2.2 μm. For J0836+0054, J1429+5447, and J0131–0321, $\alpha_{\lambda,\rm UV}$ was not directly available from the literature but we calculated it from their published spectra.

[c] To estimate $R_{2500} = f_{\nu,5\,\rm GHz}/f_{\nu,2500\,\rm Å}$, we extrapolate m_{1450} and $f_{1.4\,\rm GHz}$ to rest-frame 2500 Å and 5 GHz flux densities using the reported UV and radio slopes, respectively. For objects without $\alpha_{\lambda,\rm UV}$, we assume the median value,$\alpha_{\lambda,\rm UV,median} = -1.36$, found in the analysis of 38 $z \gtrsim 6$ quasars by Schindler et al. (2020). For objects without $\alpha_{\nu,\rm radio}$, we assume the median value from all the 'type=quasar' sources in this table: $\alpha_{\nu,\rm radio,median} = -0.67$. See section 4.1.1 for implications of extrapolating $\alpha_{\nu,\rm radio}$.

NOTE—Blazars are highly variable objects and the UV and radio properties for the objects in this list were not observed simultaneously. Therefore, the radio-loudness reported here should be treated with caution, especially for blazars.

References— 1: This work; 2: Willott et al. (2010a); 3: Wang et al. (2011); 4: Bañados et al. (2016); 5: Becker et al. (1995); 6: Shao et al. (2020); 7: McGreer et al. (2006); 8: Stern et al. (2007); 9: Shen et al. (2019); 10: Belladitta et al. (2020); 11: $y_{\rm P1}$ magnitude; 12: Condon et al. (1998); 13: Zeimann et al. (2011); 14: Liu et al. (2021); 15: Bañados et al. (2018a); 16: Fan et al. (2001); 17: Kurk et al. (2007); 18: Wang et al. (2007); 19: Saxena et al. (2018); 20: Bañados et al. (2015); 21: Drouart et al. (2020); 22: Romani et al. (2004); 23: An & Romani (2018); 24: Schneider et al. (2010); 25: Pâris et al. (2018); 26: Frey et al. (2015); 27: Wang et al. (2016); 28: Yang et al. (2016); 29: van Breugel et al. (1999); 30: Yi et al. (2014); 31: McGreer et al. (2013); 32: Hodge et al. (2011); 33: Wu et al. (2013)

Hodge, J. A., Becker, R. H., White, R. L., Richards, G. T., & Zeimann, G. R. 2011, AJ, 142, 3, doi: 10.1088/0004-6256/142/1/3
Horne, K. 1986, PASP, 98, 609, doi: 10.1086/131801
Hunter, J. D. 2007, Computing in Science and Engineering, 9, 90, doi: 10.1109/MCSE.2007.55
Intema, H. T., Jagannathan, P., Mooley, K. P., & Frail, D. A. 2017, A&A, 598, A78, doi: 10.1051/0004-6361/201628536
Ishimoto, R., Kashikawa, N., Onoue, M., et al. 2020, ApJ, 903, 60, doi: 10.3847/1538-4357/abb80b
Jiang, L., Fan, X., Ivezić, Ž., et al. 2007, ApJ, 656, 680, doi: 10.1086/510831
Jolley, E. J. D., & Kuncic, Z. 2008, MNRAS, 386, 989, doi: 10.1111/j.1365-2966.2008.13082.x
Kellermann, K. I., Sramek, R., Schmidt, M., Shaffer, D. B., & Green, R. 1989, AJ, 98, 1195, doi: 10.1086/115207
Kratzer, R. M., & Richards, G. T. 2015, AJ, 149, 61, doi: 10.1088/0004-6256/149/2/61
Kurk, J. D., Walter, F., Fan, X., et al. 2007, ApJ, 669, 32, doi: 10.1086/521596
Lang, D. 2014, AJ, 147, 108, doi: 10.1088/0004-6256/147/5/108
Leighly, K. M., & Moore, J. R. 2004, ApJ, 611, 107, doi: 10.1086/422088
Liu, Y., Wang, R., Momjian, E., et al. 2021, ApJ, 908, 124, doi: 10.3847/1538-4357/abd3a8
Matsuoka, Y., Iwasawa, K., Onoue, M., et al. 2019a, ApJ, 883, 183, doi: 10.3847/1538-4357/ab3c60
Matsuoka, Y., Onoue, M., Kashikawa, N., et al. 2019b, ApJL, 872, L2, doi: 10.3847/2041-8213/ab0216
Mazzucchelli, C., Bañados, E., Venemans, B. P., et al. 2017, ApJ, 849, 91, doi: 10.3847/1538-4357/aa9185
McGreer, I. D., Becker, R. H., Helfand, D. J., & White, R. L. 2006, ApJ, 652, 157, doi: 10.1086/507767
McGreer, I. D., Jiang, L., Fan, X., et al. 2013, ApJ, 768, 105, doi: 10.1088/0004-637X/768/2/105
McMullin, J. P., Waters, B., Schiebel, D., Young, W., & Golap, K. 2007, in Astronomical Society of the Pacific Conference Series, Vol. 376, Astronomical Data Analysis Software and Systems XVI, ed. R. A. Shaw, F. Hill, & D. J. Bell, 127
Meisner, A. M., Lang, D., Schlafly, E. F., & Schlegel, D. J. 2019, PASP, 131, 124504, doi: 10.1088/1538-3873/ab3df4
Meisner, A. M., Lang, D., & Schlegel, D. J. 2017, AJ, 154, 161, doi: 10.3847/1538-3881/aa894e
Meyer, R. A., Bosman, S. E. I., & Ellis, R. S. 2019, MNRAS, 487, 3305, doi: 10.1093/mnras/stz1504
Momjian, E., Bañados, E., Carilli, C. L., et al. 2021, AJ in press
Momjian, E., Carilli, C. L., Bañados, E., Walter, F., & Venemans, B. P. 2018, ApJ, 861, 86, doi: 10.3847/1538-4357/aac76f
Momjian, E., Carilli, C. L., & McGreer, I. D. 2008, AJ, 136, 344, doi: 10.1088/0004-6256/136/1/344
Momjian, E., Carilli, C. L., Walter, F., & Venemans, B. 2014, AJ, 147, 6, doi: 10.1088/0004-6256/147/1/6
Neeleman, M., Bañados, E., Walter, F., et al. 2019, ApJ, 882, 10, doi: 10.3847/1538-4357/ab2ed3
Noirot, G., Stern, D., Mei, S., et al. 2018, ApJ, 859, 38, doi: 10.3847/1538-4357/aabadb
Nyland, K., Dong, D. Z., Patil, P., et al. 2020, ApJ, 905, 74, doi: 10.3847/1538-4357/abc341
Oesch, P. A., Bouwens, R. J., Illingworth, G. D., et al. 2014, ApJ, 786, 108, doi: 10.1088/0004-637X/786/2/108
Onoue, M., Kashikawa, N., Matsuoka, Y., et al. 2019, ApJ, 880, 77, doi: 10.3847/1538-4357/ab29e9
Onoue, M., Bañados, E., Mazzucchelli, C., et al. 2020, ApJ, 898, 105, doi: 10.3847/1538-4357/aba193
Overzier, R. A. 2016, A&A Rv, 24, 14, doi: 10.1007/s00159-016-0100-3
Padovani, P. 2017, Nature Astronomy, 1, 0194, doi: 10.1038/s41550-017-0194
Pâris, I., Petitjean, P., Aubourg, É., et al. 2018, A&A, 613, A51, doi: 10.1051/0004-6361/201732445
Pogge, R. W., Atwood, B., Brewer, D. F., et al. 2010, in Society of Photo-Optical Instrumentation Engineers (SPIE) Conference Series, Vol. 7735, Society of Photo-Optical Instrumentation Engineers (SPIE) Conference Series, doi: 10.1117/12.857215
Pons, E., McMahon, R. G., Simcoe, R. A., et al. 2019, MNRAS, 484, 5142, doi: 10.1093/mnras/stz292
Prochaska, J., Hennawi, J., Westfall, K., et al. 2020, The Journal of Open Source Software, 5, 2308, doi: 10.21105/joss.02308
Prochaska, J. X., Hennawi, J., Cooke, R., et al. 2019, pypeit/PypeIt: Releasing for DOI, 0.11.0.1, Zenodo, doi: 10.5281/zenodo.3506873
Reed, S. L., Banerji, M., Becker, G. D., et al. 2019, MNRAS, 487, 1874, doi: 10.1093/mnras/stz1341
Richards, G. T., Vanden Berk, D. E., Reichard, T. A., et al. 2002, AJ, 124, 1, doi: 10.1086/341167
Richards, G. T., Lacy, M., Storrie-Lombardi, L. J., et al. 2006, ApJS, 166, 470, doi: 10.1086/506525
Richards, G. T., Kruczek, N. E., Gallagher, S. C., et al. 2011, AJ, 141, 167, doi: 10.1088/0004-6256/141/5/167
Romani, R. W., Sowards-Emmerd, D., Greenhill, L., & Michelson, P. 2004, ApJL, 610, L9, doi: 10.1086/423201
Runnoe, J. C., Brotherton, M. S., & Shang, Z. 2012, MNRAS, 422, 478, doi: 10.1111/j.1365-2966.2012.20620.x

Saxena, A., Marinello, M., Overzier, R. A., et al. 2018, MNRAS, 480, 2733, doi: 10.1093/mnras/sty1996
Schindler, J.-T., Farina, E. P., Bañados, E., et al. 2020, ApJ, 905, 51, doi: 10.3847/1538-4357/abc2d7
Schlafly, E. F., Meisner, A. M., & Green, G. M. 2019, ApJS, 240, 30, doi: 10.3847/1538-4365/aafbea
Schneider, D. P., Richards, G. T., Hall, P. B., et al. 2010, AJ, 139, 2360, doi: 10.1088/0004-6256/139/6/2360
Shao, Y., Wagg, J., Wang, R., et al. 2020, A&A, 641, A85, doi: 10.1051/0004-6361/202038469
Shen, Y., Richards, G. T., Strauss, M. A., et al. 2011, ApJS, 194, 45, doi: 10.1088/0067-0049/194/2/45
Shen, Y., Wu, J., Jiang, L., et al. 2019, ApJ, 873, 35, doi: 10.3847/1538-4357/ab03d9
Shimabukuro, H., Ichiki, K., & Kadota, K. 2020, PhRvD, 101, 043516, doi: 10.1103/PhysRevD.101.043516
Simcoe, R. A., Burgasser, A. J., Bernstein, R. A., et al. 2008, in Society of Photo-Optical Instrumentation Engineers (SPIE) Conference Series, Vol. 7014, Society of Photo-Optical Instrumentation Engineers (SPIE) Conference Series, doi: 10.1117/12.790414
Simcoe, R. A., Burgasser, A. J., Schechter, P. L., et al. 2013, PASP, 125, 270, doi: 10.1086/670241
Stern, D., Kirkpatrick, J. D., Allen, L. E., et al. 2007, ApJ, 663, 677, doi: 10.1086/516833
Taylor, M. B. 2005, in Astronomical Society of the Pacific Conference Series, Vol. 347, Astronomical Data Analysis Software and Systems XIV, ed. P. Shopbell, M. Britton, & R. Ebert, 29
Thyagarajan, N. 2020, ApJ, 899, 16, doi: 10.3847/1538-4357/ab9e6d
van Breugel, W., De Breuck, C., Stanford, S. A., et al. 1999, ApJL, 518, L61, doi: 10.1086/312080
Venemans, B. P., Röttgering, H. J. A., Miley, G. K., et al. 2007, A&A, 461, 823, doi: 10.1051/0004-6361:20053941
Venemans, B. P., Bañados, E., Decarli, R., et al. 2015, ApJL, 801, L11, doi: 10.1088/2041-8205/801/1/L11
Vernet, J., Dekker, H., D'Odorico, S., et al. 2011, A&A, 536, A105, doi: 10.1051/0004-6361/201117752
Vestergaard, M., & Osmer, P. S. 2009, ApJ, 699, 800, doi: 10.1088/0004-637X/699/1/800
Vestergaard, M., & Wilkes, B. J. 2001, ApJS, 134, 1, doi: 10.1086/320357
Virtanen, P., Gommers, R., Oliphant, T. E., et al. 2020, Nature Methods, 17, 261, doi: 10.1038/s41592-019-0686-2
Vito, F., Brandt, W. N., Bauer, F. E., et al. 2019, A&A, 628, L6, doi: 10.1051/0004-6361/201935924
Volonteri, M., Silk, J., & Dubus, G. 2015, ApJ, 804, 148, doi: 10.1088/0004-637X/804/2/148
Wang, F., Wu, X.-B., Fan, X., et al. 2016, ApJ, 819, 24, doi: 10.3847/0004-637X/819/1/24
Wang, F., Davies, F. B., Yang, J., et al. 2020, ApJ, 896, 23, doi: 10.3847/1538-4357/ab8c45
Wang, R., Carilli, C. L., Beelen, A., et al. 2007, AJ, 134, 617, doi: 10.1086/518867
Wang, R., Wagg, J., Carilli, C. L., et al. 2011, ApJL, 739, L34, doi: 10.1088/2041-8205/739/1/L34
Willott, C. J., Delorme, P., Reylé, C., et al. 2010a, AJ, 139, 906, doi: 10.1088/0004-6256/139/3/906
Willott, C. J., Albert, L., Arzoumanian, D., et al. 2010b, AJ, 140, 546, doi: 10.1088/0004-6256/140/2/546
Wilson, J. C., Henderson, C. P., Herter, T. L., et al. 2004, in Society of Photo-Optical Instrumentation Engineers (SPIE) Conference Series, Vol. 5492, Ground-based Instrumentation for Astronomy, ed. A. F. M. Moorwood & M. Iye, 1295–1305, doi: 10.1117/12.550925
Wu, J., Brandt, W. N., Miller, B. P., et al. 2013, ApJ, 763, 109, doi: 10.1088/0004-637X/763/2/109
Wu, J., Ghisellini, G., Hodges-Kluck, E., et al. 2017, MNRAS, 468, 109, doi: 10.1093/mnras/stx416
Wu, X.-B., Wang, F., Fan, X., et al. 2015, Nature, 518, 512, doi: 10.1038/nature14241
Wylezalek, D., Galametz, A., Stern, D., et al. 2013, ApJ, 769, 79, doi: 10.1088/0004-637X/769/1/79
Yang, J., Wang, F., Wu, X.-B., et al. 2016, ApJ, 829, 33, doi: 10.3847/0004-637X/829/1/33
Yang, J., Wang, F., Fan, X., et al. 2020, ApJL, 897, L14, doi: 10.3847/2041-8213/ab9c26
Yi, W.-M., Wang, F., Wu, X.-B., et al. 2014, ApJL, 795, L29, doi: 10.1088/2041-8205/795/2/L29
Zeimann, G. R., White, R. L., Becker, R. H., et al. 2011, ApJ, 736, 57, doi: 10.1088/0004-637X/736/1/57